Journal of Biomedical Optics

SPIEDigitalLibrary.org/jbo

Magnetic-field-assisted photothermal therapy of cancer cells using Fe-doped carbon nanoparticles

Ling Gu
Vijaylakshmi Vardarajan
Ali R. Koymen
Samarendra K. Mohanty

SPIE

Magnetic-field-assisted photothermal therapy of cancer cells using Fe-doped carbon nanoparticles

Ling Gu Vijaylakshmi Vardarajan Ali R. Koymen and Samarendra K. Mohanty
University of Texas at Arlington, Department of Physics, Texas 76019

Abstract. Photothermal therapy with assistance of nanoparticles offers a solution for the destruction of cancer cells without significant collateral damage to otherwise healthy cells. However, minimizing the required number of injected nanoparticles is a major challenge. Here, we introduce the use of magnetic carbon nanoparticles (MCNPs), localizing them in a desired region by applying an external magnetic-field, and irradiating the targeted cancer cells with a near-infrared laser beam. The MCNPs were prepared in benzene, using an electric plasma discharge, generated in the cavitation field of an ultrasonic horn. The CNPs were made ferromagnetic by use of Fe-electrodes to dope the CNPs, as confirmed by magnetometry. Transmission electron microscopy measurements showed the size distribution of these MCNPs to be in the range of 5 to 10 nm. For photothermal irradiation, a tunable continuous wave Ti: Sapphire laser beam was weakly focused on to the cell monolayer under an inverted fluorescence microscope. The response of different cell types to photothermal irradiation was investigated. Cell death in the presence of both MCNPs and laser beam was confirmed by morphological changes and propidium iodide fluorescence inclusion assay. The results of our study suggest that MCNP based photothermal therapy is a promising approach to remotely guide photothermal therapy. [DOI: 10.1117/1.JBO.17.1.018003]

Keywords: carbon nanoparticle; magnetic nanoparticle; cancer; photothermal therapy.

Paper 11254P received May 21, 2011; revised manuscript received Nov. 22, 2011; accepted for publication Nov. 23, 2011; published online Feb. 6, 2012.

1 Introduction

Nanoscale objects are finding extensive use in combating cancer via a comprehensive approach, namely drug delivery,[1–3] photothermal therapy,[4,5] and detection of circulating cancer cells.[6,7] The development of novel nanoparticles has led to a dramatic increase in photothermal therapy as a minimally invasive treatment modality for the treatment of cancer cells, bacteria, viruses, and deoxyribonucleic acid (DNA) targeted with nanoparticles. Photothermal therapeutic agents are usually developed to have strong absorption around a selected wavelength to avoid the competition of light absorption by native tissue chromophores that will reduce the effectiveness of heat deposition within malignant cells and increase non targeted injury to adjacent healthy tissues. Carbon nanotubes[8,9] and gold nanostructures, which are able to overcome limitations of traditional dye-based photothermal molecules, such as low absorption and photobleaching under laser irradiation,[10] has shown good promise for photothermal therapy due to their strong absorption in the visible and near-infrared (NIR) regions on account of their surface plasmon resonance oscillations. While the toxicity of carbon nanotubes is still under debate,[11–13] change in shape of the gold nanorods due to heating upon NIR irradiation may reduce their clinical efficacy in case of repeated irradiation schedules. Although functionalization of these nanoparticles is necessary for receptor-mediated internalization into the cells for efficient delivery, for photothermal therapy, internalization of nanoparticles is not a major requirement. Enhanced permeation and retention (EPR) effect due to leaky vasculature in tumor and poor lymphatic drainage can be a major factor for retention of nanoparticles.[14] Since vascular pore size is generally few 100 nm (except in few cases where it can be larger),[14,15] size of nanoparticles need to be smaller than the size of the renal excretion threshold. Further, nanostructures having large sizes lead to their rapid clearance by the reticuloendothelial system upon intravenous injection.[16] Unless chemically functionalized, the randomly localized small (<10 nm) gold and carbon nanostructures make it difficult to be efficiently retained and heat the tumor region in a highly specific manner.

Magnetic nanoparticles are attractive due to the fact that they can be captured and concentrated in target areas by an external magnetic-field and therefore emerging as a viable technology for *in-vivo* drug delivery.[17] Recently, alternating and very high magnetic-field in radiofrequency range have been applied[18–20] to cause effective absorption of the energy for therapeutics purpose. However, no report exists on photothermal therapy using magnetically localized photo-absorbing magnetic carbon nanoparticles. Here, we report this hybrid approach to magnetic-field-assisted photothermal therapeutics using magnetic carbon nanoparticles (MCNP) having a strong absorption in NIR (700 to 1000 nm) biological window. It may be noted that CNPs are less toxic than carbon nanotubes.[21,22] The method of irradiation of MCNPs with NIR continuous wave (cw) laser beam is applied to photothermal treatment of variety of cancer cells (human prostate cancer cells and human fibroblast sarcoma cells). Application of external magnetic-field led to localization of the MCNPs in the region of interest, which significantly

Address all correspondence to: Samarendra K. Mohanty, Biophysics and Physiology Group, Department of Physics, University of Texas at Arlington, 502 Yates Street, 108 Science Hall, Arlington, TX 76019. Tel: 817-272-1177; Fax: +1-817-272-3637; E-mail: smohanty@uta.edu

0091-3286/2012/$25.00 © 2012 SPIE

reduced the required dose of the laser beam for achieving similar therapeutic effects.

2 Materials and Methods

2.1 *Synthesis of Magnetic CNP*

MCNPs were synthesized at ~4 kV in liquid benzene (Sigma Aldrich) using the electric plasma discharge generated between two iron electrodes in the cavitation field of an ultrasonic horn (VCX 750, Sonics). The two Fe-electrodes were placed ~0.7 mm apart and 1 cm beneath the ultrasonic horn. The ultrasonic horn was used at 600 W and 20 kHz in 100 ml of liquid benzene. After ~1 hour, black carbon powder was produced by dissociation of benzene molecules leading to change in the color of the liquid benzene. The powder was separated by centrifugation from the benzene, dispersed in ethanol, and dried in a vacuum oven at 313 K. During the plasma formation, Fe-electrodes erode and 1 to 2% of Fe gets embedded into the carbon matrix, making them magnetic.

2.2 *Size and Structural Characterization of MCNP by TEM*

A high resolution transmission electron microscope (HRTEM, H-9500, Hitachi) was used to study the particle size and structure of the MCNPs. The TEM samples were prepared by placing one drop of the MCNP solution in distilled water onto a carbon coated mesh copper TEM grid.

2.3 *Measurement of Magnetization*

The magnetic properties of MCNPs were measured by using a vibrating sample magnetometer (VSM, Lakeshore) at room temperature using an applied magnetic-field ranging from −15 kOe to +15 kOe. Magnetic measurements showed that the MCNP powder sample is ferromagnetic with a low ratio of remnant to saturation magnetization.

2.4 *Absorption Measurement*

Absorption measurements were made by a spectrophotometer (Lambda EZ 210, Perkin-Elmer). MCNP powder was diluted in D_2O. The absorption of the MCNPs was measured in D_2O in order to avoid water absorption peaks in NIR. The MCNP solution was ultra-sonicated for an hour before absorption measurement. The reference was taken with D_2O solution in a quartz cell of 1 cm path length and absorption spectrum of the well-dispersed sample was measured over NIR wavelength range (700 to 1000 nm). The sample was continuously diluted to a final concentration of 28 μg/ml so as to avoid scattering tail.

2.5 *Cell Culture and Incubation with MCNPs*

Human prostate cancer (PC3) cells and human fibroblast sarcoma (HT1080) cells were routinely cultured in Dulbecco's modified Eagle's medium (DMEM) supplemented with 5% fetal bovine serum (FBS). The cultures were maintained at 37°C in a 5% CO_2 humidified atmosphere. For photothermal treatment, cells were trypsinized, plated on glass coverslip-bottom dishes and used after 24 hours of culturing. MCNPs were added into culture media to a final concentration of 25 μg/ml and incubated at 37°C in a 5% CO_2 humidified atmosphere for 3 hours before experiment. DMEM and FBS were purchased from Lonza (MD, US). Trypsin was purchased from Mediatech (Manassas, USA). All other reagents were purchased from Fisher Scientific, except those specifically mentioned.

2.6 *MTT Assay*

To determine cell viability, MTT (Biosynth International Inc., Switzerland) assay was used. Briefly, cells were trypsinized and plated into 96-well plate and then were treated with MCNPs with different concentration and incubation period. MTT (25 μl, 5 mg/ml), dissolved in PBS, was added into each well. After 4-hour incubation at 37°C, MTT was removed and 100 μl DMSO was added. The absorbance was measured at 570 nm wavelength and background at 650 nm wavelength was subtracted.

2.7 *NIR Laser Beam Irradiation and Cell Imaging*

A schematic of the laser beam irradiation and imaging set up is shown in Fig. 1. A cw Ti: Sapphire laser (Maitai HP, Newport Spectra-Physics Inc.) beam in mode-lock off condition with a wavelength tuning range from 690 to 1040 nm was directed toward the sample through an inverted optical microscope (Ti-U, Nikon). A 20X objective (MO, NA = 0.5) was used to focus the laser beam to diffraction limited spot for photothermal irradiation. The dichroic mirror 1 (DM1) combined the laser beam and the beam from the excitation source. The dichroic mirror 2 (DM2) reflects the excitation lamp light and transmits the emitted fluorescence to the CCD. The emission filter (Em) blocked the laser NIR wavelength. Bright-field and fluorescence images were captured with exposure of 100 ms using a cooled

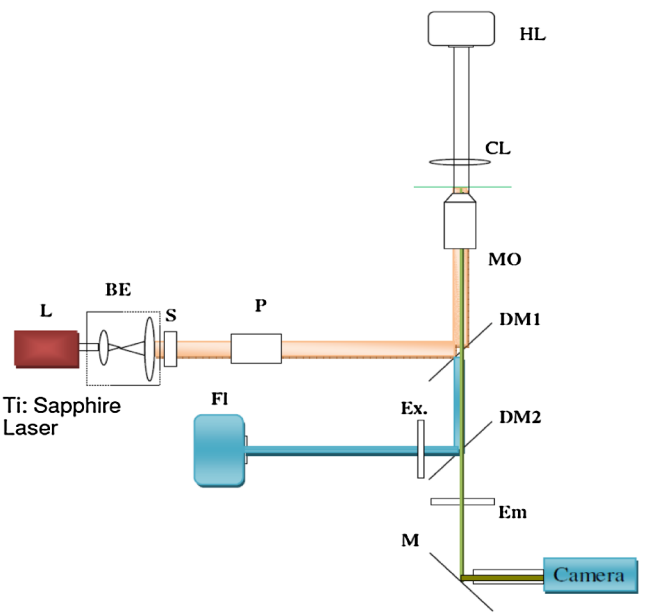

Fig. 1 Experimental set-up for photothermal irradiation. L: Ti: Sapphire Laser; BE: Beam Expander; S: Uniblitz Shutter; P: Polarizer; Fl.: Fluorescence excitation source; Ex: Excitation Filter; Em: Emission Filter; MO: Microscope Objective; CL: Condenser lens; DM1 and DM2: Dichroic Mirrors; M: Mirror; HL: Halogen Lamp.

CCD camera (Coolsnap ES, Photometrics Inc.) and processed using ImageJ software. The exposure time (0 to 20 s) was controlled by a mechanical shutter (*S*, Uniblitz).

Once magnetic-field is applied for few hours to localize the nanoparticles on cells in the incubator, the petridish was placed under microscope. Cells were stained with Calcein (1 μM, Invitrogen) at 37°C for 15 min before experiment. Propidium iodide (PI, 5 μM) was added immediately before viewing under inverted fluorescent microscope (Nikon Ti-U) using the 20X objective. The laser beam power at the sample plane was measured using a power meter (PM100D, Thorlabs). The power of the laser beam was varied (20 to 100 mW) by controlling the angle of orientation of a Glan-Thompson polarizer (*P*) in the beam path. The XY-scanning of the region of interest (to be irradiated by the laser beam) was achieved by controlling the motorized sample stage movement. Live-dead assay was conducted to determine viability of cells surrounding the irradiation zone. Inclusion of Calcein and exclusion of PI, respectively, indicates live and dead cell. PI is a membrane impermeable nuclear stain which has characteristic red fluorescence. To irradiate the cells under microscope with the laser beam while applying the magnetic-field simultaneously, suitable ring magnet can be used to allow the optical path for optical imaging and irradiation.

2.8 *Theoretical Calculation of the Local Temperature Rise Photothermal Therapy*

The local temperature rise as a result of the laser heating of MCNPs was calculated on the basis of a numerical model. The laser-heated MCNPs were assumed to be the only point sources of heat on the cellular matrix. Evaporation of water as a cooling mechanism was neglected. The temperature rise in the cell was estimated by considering two concurrent processes: heat generation in the MCNPs by absorption of the laser beam and heat depletion into the surrounding media by the process of conduction. Accordingly, these two processes were modeled in spherically symmetric coordinates into the Fourier heat equation,[23]

$$\rho c\left(\frac{\partial T}{\partial t}\right) = \frac{k}{r^2}\frac{\partial}{\partial r}\left(r^2\frac{\partial T}{\partial r}\right) + Q_s, \quad (1)$$

where T is the temperature (K), ρ is the cell density (kg/m^3), c is the specific heat capacity of the cells ($J\,kg^{-1}\,K^{-1}$), k is the thermal conductivity of the cells and their medium ($W\,m^{-1}\,K^{-1}$), t is the time (s), Q_s is the heat-source term (W/m^3) due to the MCNPs heated by the continuous wave laser excitation and r is the radial distance (m) from the heated MCNPs. Assuming that 100% of the energy absorbed by the MCNPs is transferred to the surroundings as heat, Using Beer–Lambert's law: $A = -\log(1 - Q_s/Q) = \varepsilon cl$, A: absorbance of the MCNPs; Q is the incident laser power per unit volume (W/m^3) in the focal spot, ε: extinction coefficient; c: concentration of MCNP; l: path length), Q_s becomes equal to the laser power absorbed by the MCNPs per unit volume;

$$Q_s = Q(1 - 10^{-A}). \quad (2)$$

Absorption of the laser energy directly by the cells was neglected due to their extremely low absorption cross section at NIR as compared to that of MCNPs. Further, the scattering component of the extinction by 10 nm MCNPs was neglected in comparison to their much higher absorption. The thermal properties of the cells were derived following the established relationships:[24] $c = 4190(0.37 + 0.63M_W)\ J\,kg^{-1}\,K^{-1}$ and $k = 4190(0.13 + 1.36M_W)\ W\,m^{-1}\,K^{-1}$ where M_W is the water mass content of the cells. Assuming a density of $1.3 \times 10^3\ kg\,m^{-3}$ for dry cells, the density of the cells was estimated[25] as $\rho = (1300 - 300M_W)\ kg\,m^{-3}$. For a water mass content of 70%, the values were thus: $\rho = 1090\ kg\,m^{-3}$, $k = 0.45\ W\,m^{-1}\,K^{-1}$ and $c = 3370\ J\,kg^{-1}\,K^{-1}$.[26] The ambient temperature T_o was set at 27°C. The heating control volume (m^3) for the calculation was based on the radius of focal spot ($R = 1$ μm) and path length l (depth of focus $= 2\pi R^2/\lambda$) of 8 μm.

The heat transport equation was solved by an explicit finite-difference method given by

$$\rho c\left(\frac{T_{i+1\,j} - T_{ij}}{\Delta t}\right) = k\left(\frac{T_{ij-1} - 2T_{ij} + T_{ij+1}}{(\Delta r)^2}\right) + Q_s, \quad (3)$$

where Δt and Δr are the characteristic time and distance steps, and i and j are the corresponding indices. A stability criterion[23] for the finite-difference method is given by

$$\Delta t \le \frac{2\rho c(\Delta r)^2}{K}, \quad (4)$$

thus imposing a constraint on the value of Δt for a selected value of Δr. A decrease in Δr affords a higher accuracy, but at the expense of a quadratic increase in the number of time-step computations. The distance step Δr was selected to be 1 nm, whereas Δt was evaluated (to be 40.8 ns) from the limiting condition of the stability criterion.

3 Results and Discussion

3.1 *Structural, Magnetic and Absorption Characteristics of MCNPs*

Figure 2(a) shows the HRTEM image of a cluster of carbon nanoparticles prepared at ~4 kV using Fe-electrodes. The average size of the nanoparticles was found to be in the range of 5 to 10 nm. Further, the CNPs were found to be crystalline (Fig. 2(a)). Magnetic measurements (Fig. 2(b)) showed that the MCNP powder sample is ferromagnetic with a low ratio of remanent to saturation magnetization. This allowed the MCNPs in solution to be attracted to an external magnetic-field (inset in Fig. 2(b), magnet removed just before taking the picture). Absorption spectroscopic measurements (Fig. 3(a)) of the MCNPs showed significant absorption in the NIR region. Though 850 nm has strongest absorption, the experiments were carried out at 720 and 800 nm due to the fact that our Ti: Sapphire laser was operating more stably in cw mode (in mode-lock off condition) at these wavelengths, and we wanted to verify if small change in MCNP-absorbance has any distinct effect on photothermal efficacy. Use of 850 nm is expected to enhance the effectiveness of the method. The MCNPs are highly non-reactive due to their crystalline structure (Fig. 2(a)) and stable in water as well as physiological solutions for several months. The absorbance at

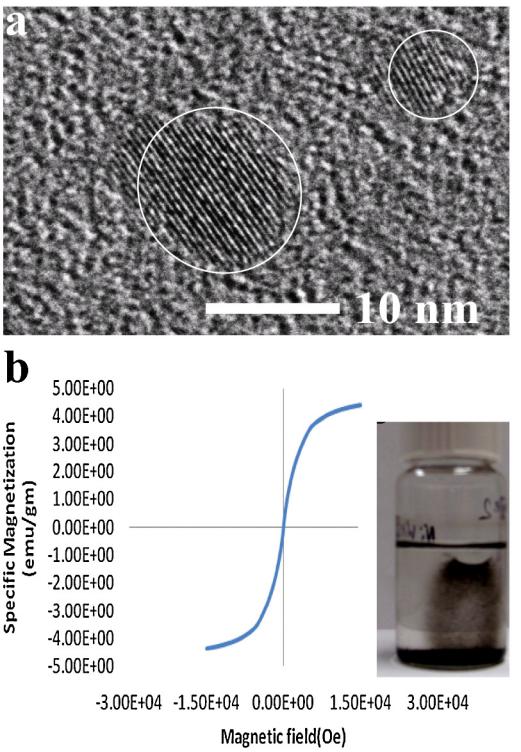

Fig. 2 (a) HRTEM images of two MCNPs prepared at ~4 kV using iron electrodes, (b) Magnetization measured from the MCNP powder with a VSM at room temperature. Inset shows accumulation of MCNPs to one side of the bottle under external magnetic-field.

800 and 720 nm was measured to be 0.0115 and 0.0095, respectively. Using Beer–Lambert's law ($A = -\log I/I_0 = \varepsilon cl$, A: absorbance; ε: extinction coefficient, c: concentration of MCNP; l: path length), the extinction coefficient at 800 nm and 720 nm was estimated to be 0.411 ml.mg^{-1} cm^{-1} and 0.339 ml.mg^{-1} cm^{-1} respectively.

The temperature change in the immediate vicinity of the heated MCNP was theoretically estimated for different MCNP concentrations and shown in Fig. 3(b). As shown in Fig. 3(b), the temperature of cell membrane in immediate vicinity of MCNPs was found to increase with laser irradiation time. At laser irradiation wavelength of 800 nm and power of 50 mW, the temperature rise is ~40 K for a concentration of 1.4 ml.mg as compared to only 8 K for 280 μg/ml. The temperature rise can be as high as 80 K for higher concentration (2.8 mg/ml). Further, the saturated peak temperature rise (Fig. 3(b)) was found to increase linearly with the power of the laser beam. The spatial distribution of temperature around the MCNP (after 0.4 s irradiation) showed that the temperature decreases with increasing distance from the MCNP center.

3.2 *MCNPs Localized Over Cells Under External Magnetic-Field*

An assembly of Neodymium Iron Boron magnets was used to introduce magnetic-field on to cells during incubation of cells with MCNPs. The schematic of magnetic lines of force on the MCNPs is shown in Fig. 4(a). The magnetic force near the center of the magnet was measured to be much higher than that at 5 mm away from the center using a Gauss meter. Figure 4(b) shows the actual setup for concentrating the

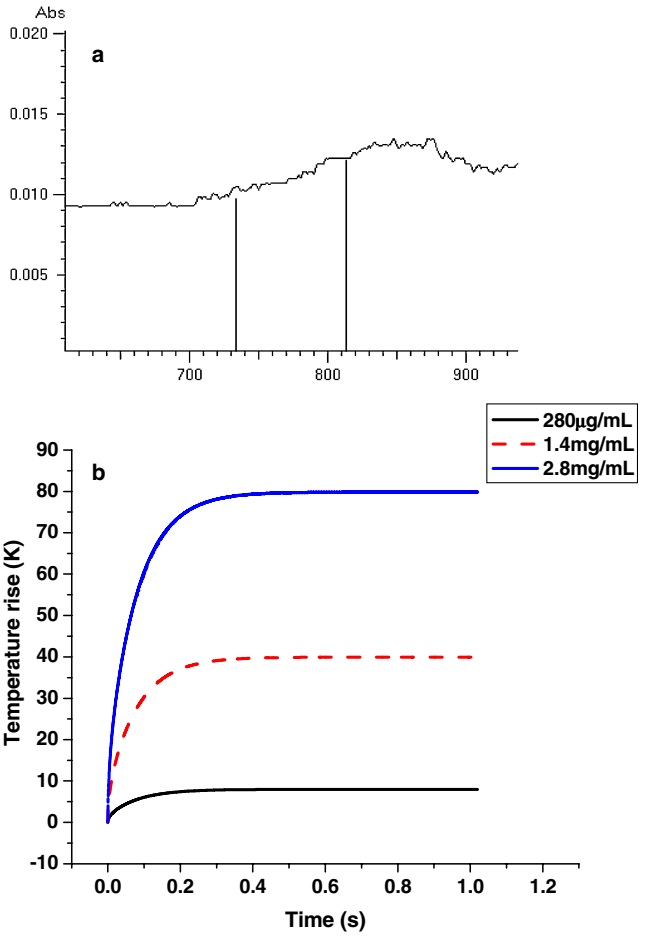

Fig. 3 (a) Absorption spectrum of MCNPs at 28 μg/ml. (b) Theoretical calculation of temperature rise in the focal volume of the laser beam (50 mW) at varying concentration of MCNPs.

MCNPs on cells in monolayer. Consequently, the concentration of MCNPs at the tip (Fig. 4(c)) of the external magnet was found to be significantly higher than that at 5 mm away from the center of the magnet (Fig 4(d)) as well. Thus, the MCNPs could be selectively concentrated using an external magnetic-field, which can be extended to *in-vivo* applications for targeting the MCNPs to the tumor region so that they can be irradiated without damaging normal cells. Figure 4(e) and (f) show the binary images corresponding to (c) and (d), respectively. Converting the bright-field images to binary images allowed estimation of magnetic-field-assisted enhancement of nanoparticles' concentration from the mean value (124 and 3 corresponding to image (e) and (f)). The temperature simulation (Fig. 3(b)) shows that at laser power of 50 mW, the temperature rise is ~4 K for a concentration enhancement factor of 50 (1.4 mg/ml) as compared to only 8 K for enhancement factor of 10 (280 μg/ml).

3.3 *Cytotoxicity of MCNPs*

To ensure that cw NIR laser beam does not induce photothermal injury of cells without attached MCNPs, cells were irradiated without MCNPs using a 720 nm laser beam at power of 92 mW up to 2 min. None of the cells ($n = 8$ for HT1080 and $n = 6$ for PC3 cells) were damaged at this dose as determined by propidium iodide exclusion assay. Figure 5 shows bright-field and live-dead staining before (a) to (c) and after

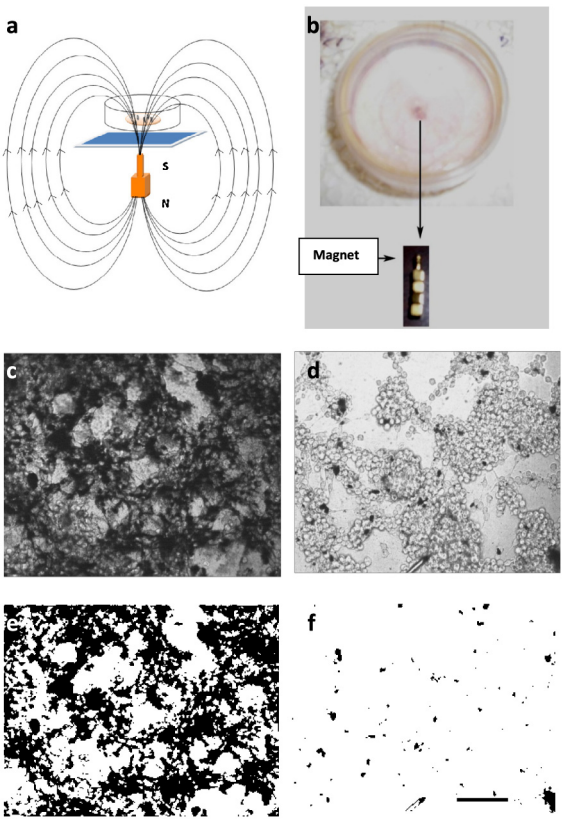

Fig. 4 Accumulation of MCNPs on cells under magnetic-field. (a) Schematic showing magnetic lines of force on MCNPs; (b) Actual setup for incubation of cells with MCNPs and external magnet; MCNPs accumulation on cells (c) near center of the magnet; (d) 5 mm away from the center. (e, f) Binary images of c & d respectively. All images are in same magnification, scale bar: 100 μm.

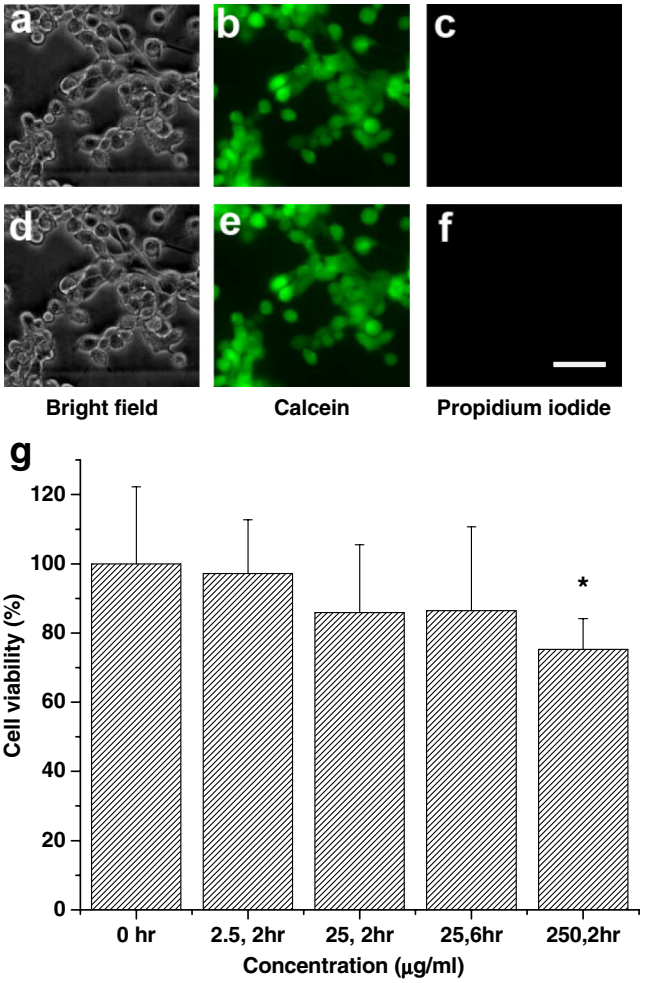

Fig. 5 Cell viability in response to laser irradiation (without MCNP) and MCNP incubation (without laser irradiation). Bright-field and live (Calcein)-dead (PI) staining before (a to c) and after laser irradiation (d to f) in absence of MCNPs. All images are in same magnification, scale bar: 50 μm. (g) Cell viability at varied concentration of MCNPs and incubation period, measured by MTT-assay, $p < 0.05$ w.r.t. 0 hr.

laser irradiation (d) to (f) in absence of MCNPs. While retention of Calcein (green fluorescence) indicates live cell, inclusion of PI confirms cells being dead. These results demonstrate that the used cw laser power does not elicit injury to cells without MCNPs, thus provide high specificity.

As shown in Fig. 5(g), cytotoxicity of MCNPs (without laser irradiation) with different concentration and incubation time were determined by MTT assay. While higher concentration of nanoparticles (250 μg/ml) decreased the viability of cells ($p < 0.05$), lower concentration (2.5 μg/ml and 25 μg/ml) of MCNPs incubated for as long as 6 hr did not significantly decrease the viability of cells. Therefore, we used 25 μg/ml of MCNPs for the magnetic-field-assisted photothermal therapy.

3.4 *Photothermal Destruction of MCNP-Targeted Cells*

When cells, after three hours of incubation with MCNPs, were irradiated using a 720 nm laser beam (92 mW), photothermal effects were evident at this power level, even at much lower exposure (0.2 s) than used for cells only (2 min, Fig. 5(a)–(f), without MCNPs). Magnetic-field-assisted photothermal destruction of targeted HT1080 cells using NIR laser beam (92 mW, 0.2 sec) is shown in Fig. 6. Based on the power level of the laser beam, laser-induced temperature rise in presence of MCNPs led to two distinct mechanisms of damage, (i) bubble formation and (ii) direct membrane damage. It may be noted that while bubble formation may not be the traditional photothermal method for destroying tumor, use of pulsed laser beam and absorbing nanoparticles for bubble formation has shown potential for selective damage of cancer cells.[27–29]

Bubble formation near irradiation site initiated, which expanded upon further exposure of the cw laser beam. Such disruptive events led to targeted destruction of cancer cells. While power level below 48 mW did not induce bubble formation, higher laser power induced bubble formation. At lower power levels (<50 mW), bubble formation was observed only in presence of cluster of MCNPs. The bubble formation caused damage over a large number of cells around the irradiation spot. Most of the cases, bubbles were formed immediately (<50 ms) after laser irradiation (13 out of 15 cells, within 40 ms). This indicates that induction of bubble is dependent on both laser beam power and size of MCNP. However, bubble size increased with increase in exposure time, and therefore, it determines the number of cells damaged per point irradiation. It is important to note here that the bubble formation, reported here, required only a continuous wave laser beam as compared to pulsed beam reported earlier.[27,28]

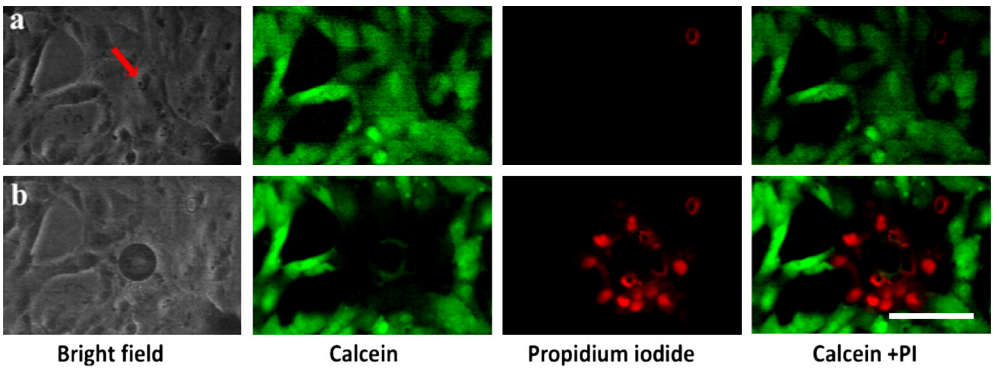

Fig. 6 Magnetic-field-assisted photothermal destruction of targeted HT1080 cells using bubble formed at high power cw NIR laser beam. Live-dead staining (a) before laser irradiation and (b) after bubble formation. All images are in same magnification, scale bar: 50 μm.

When lower dose (50 mW, 2 sec) of laser beam was applied on MCNP-bound cells (Fig. 7(a)), the temperature rise due to nanoparticles damaged the cell membrane, making the cell dead without bubble formation. Scanning of the stage in a XY region led to destruction of most of the cells in the scanned area (Fig. 7(b) & (c)). Live-dead staining confirmed cell death in laser-irradiated region at center of field of view marked by square (Fig. 7(b)). Figure 7(c) shows destruction of cells in the rectangular irradiation zone.

3.5 *Power and Wavelength Dependent Efficiency of Magnetic-Field-Assisted Photothermal Therapy*

Induction of bubble using cw laser beam (92 mW, 0.2 sec) indicates temperature rise larger than 100°C, which is in proportion to the estimated temperature rise at 50 mW with MCNP concentrated to 2.8 mg/ml (Fig. 3). Since absorption coefficient of MCNP has wavelength dependence with more absorption at 800 nm than at 720 nm, magnetic-field-assisted, wavelength-dependent photothermal destruction of cells was examined. Figure 8 shows the effect of power and wavelength of laser beam on rate of cell death, indicated by appearance time of PI fluorescence. With increase in laser power, the time required for appearance of PI fluorescence decreased for both the wavelengths. No significant wavelength dependence was observed for exposure time (or dose) at higher power levels (>50 mW). However, for power levels below 50 mW, the exposure time to cause detectable damage was found to be significantly lower for 800 nm as compared to 720 nm. The different doses required for MCNP-assisted damage at different wavelengths suggest that 800 nm is more efficient for MCNP-assisted photothermal therapy. It may be noted that these carbon

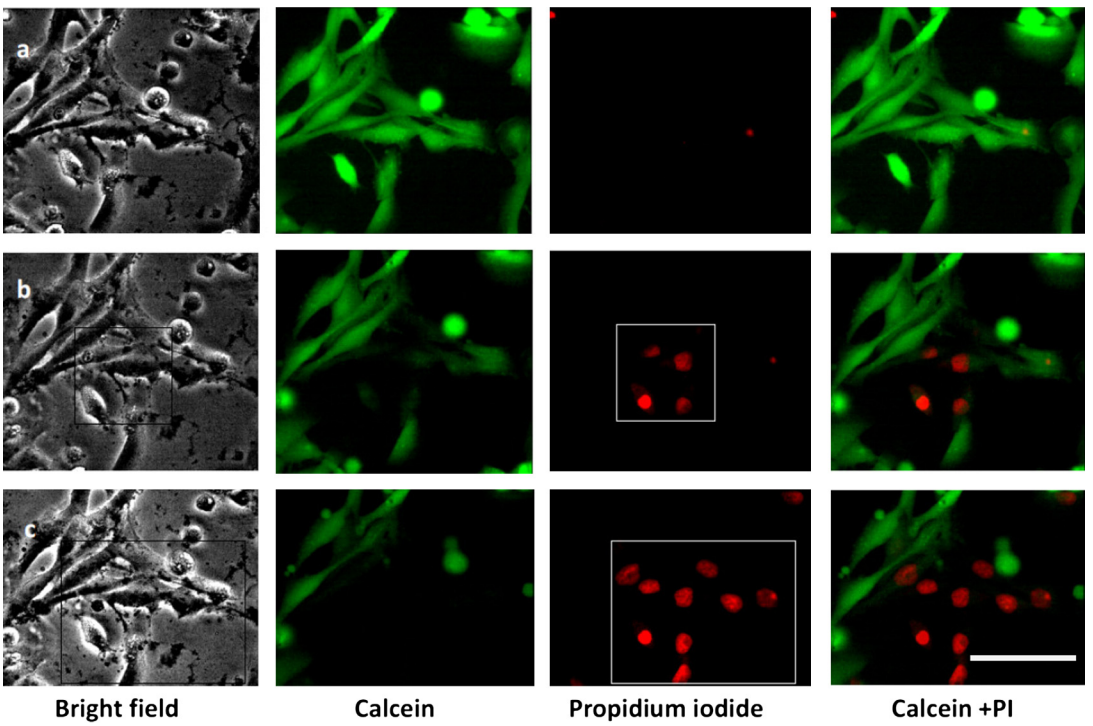

Fig. 7 Magnetic-field-assisted photothermal destruction of targeted HT1080 cells using low power cw NIR laser beam. Live-dead staining (a) before laser irradiation; (b) after irradiation in the region at center of field of view marked by square and (c) after irradiating the rectangular region. All images are in same magnification, scale bar: 50 μm.

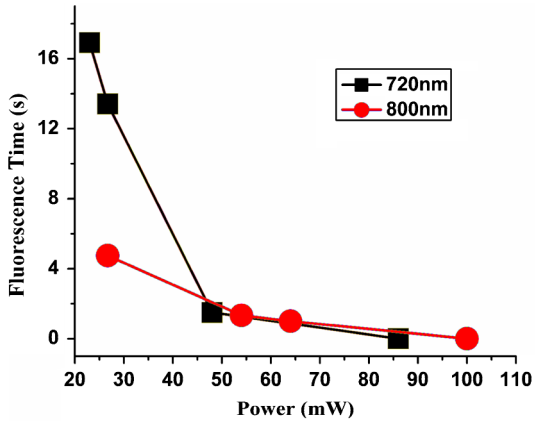

Fig. 8 Effect of power and wavelength of laser beam on rate of cell death (PI fluorescence appearance time).

nanoparticles are crystalline (as confirmed by high resolution TEM and Raman spectroscopy) having a mixture of graphite and diamond like structure. The photothermal properties,[30] such as thermal conductivity, of these carbon nanostructures are significantly higher (100–2000 W/mK) as compared to amorphous carbon nanoparticles (0.01–0.1 W/mK). Comparative studies are underway to evaluate the efficiency and wavelength dependency of other magnetic carbon nanoparticles. Since the power requirements were reduced significantly by use of external magnetic-field, it is possible to apply laser beam to a targeted region *in-vivo* for selective damage to MCNP-attached cells.

Magnetic nanoparticles can be dispersed into suitable solvents with proper surface coating, forming homogeneous suspensions that can interact with an external DC magnetic-field and be positioned to a specific area facilitating laser beam assisted cancer therapy. Our hybrid approach of magnetic-field-assisted photothermal therapy requires irradiation of MCNPs with cw laser beam in NIR wavelength band, in which biological tissue has least scattering and absorption. Delivery and retention of nanoparticles into tumor tissue has been considered as a problem in photothermal treatment. It is difficult to prevent the diffusion of nanoparticles out of the targeted area. Since the external magnetic-field increased retention of the MCNPS in targeted region, binding to cancer cells in specific regions can be increased. By use of peptide or antibody conjugation of MCNPs, even specific cell types can be targeted. Once the magnetic nanoparticles coupled with antibodies are forced to localize in the target tissues by external magnetic-field just after injection, bioconjugation can help in binding of the nanoparticles in specific cell type in the targeted region and thus be retained in specific sites *in-vivo* so as to effectively transform light into localized heat. The use of very small MCNPs (5 nm) used in this study will allow better diffusion of the nanoparticles into deep targeted tissue. Bubble formation observed at low power of cw laser beam has distinct advantages over use of femtosecond laser for photothermal therapy of tumor cells.[31] Beside being cost effective, the collateral tissue damage will be expected to be minimal in case of cw laser beam as femtosecond laser beam has a high peak power which can cause cell damage.[32] Based on absorption spectrum of different MCNPs, specific NIR wavelength can be used to cause the most damage as in our present case 800 nm and above is more effective as compared to 720 nm. Future work includes use of peptide[33] coated MCNPs to improve the efficiency of targeting prostate tumor cells.

During the irradiation by a laser beam, a spatial temperature gradient is expected to occur in the sample, and only the cells in the area above a certain threshold temperature would be damaged by the laser beam. In previous cases of photothermal irradiation of cells (incubated with gold nanorods[34] and shells[35]) with collimated beam for few minutes, theoretical prediction[34] as well as viability assay[35] showed destruction of cells only within the beam radius, suggesting little effect of heat diffusion. In our case, the damaged (rectangular) region was also very well confined to irradiated area (Fig. 7). Further, the photothermal destruction effect occurred within few sec of irradiation. This is due to the high intensity of laser beam used in our case as compared to collimated beam and in agreement with the simulation (Fig. 3), where the temperature rise at the beam focus was found to saturate within 1 sec of irradiation. Factors such as heat diffusion, laser intensity, exposure time, and the thermal properties of the sample will affect the size of the photothermal destruction area, and clearly more analysis and comparison of data with other photothermal agents[34,35] will be required for further characterization of the spatio-temporal destruction process.

Though it is feasible to apply hybrid field (magnetic-field for concentrating and light for photothermal effect) in superficial organs and in small animals, it may find difficulties for real-time clinical applications because of the complexities involved in designing a high power focused magnetic-field, and the time required to localize therapeutic levels of nanoparticles. Use of Halbach cylinder[36] will extend the penetration depth of the magnetic-field so as to allow reduction of time required for localization in *in-vivo* condition. Once nanoparticles are localized in deep seated organ sites, optical fiber can be used to deliver NIR light for efficient photothermal therapy. Further, by use of novel light beams (e.g., non-diffracting Bessel beams), deeper penetration[37,38] can be achieved as compared to conventional Gaussian beams.

4 Conclusions

We demonstrated first use of external magnetic-field-assisted accumulation of magnetic CNPs (with significant absorption properties in the NIR spectrum of biological window) for photothermal destruction of cells. Cell death in the presence of both MCNPs and laser beam was confirmed by morphological changes and propidium iodide fluorescence inclusion assay. The increased retention of the carbon nanoparticles led to reduction of volume of nanoparticles required to be injected for similar dose-dependent photothermal effect, thus providing a method to reduce cytotoxicity. While use of very small MCNPs (~5 nm) will allow easy delivery into deep targets, bioconjugation of these MCNPs will further improve retention in addition to external DC magnetic-field. The results of this study suggest that external magnetic-field-assisted photothermal therapy will significantly improve efficacy of the existing photothermal procedures.

Acknowledgments

The authors would like to thank Prof. David Gilley, Indiana University-School of Medicine for the HT1080 cells, and

Prof. Jiang Yang, University of Texas-Arlington for the PC3 cells. The authors would also like to thank Prof. Yaowu Hao, University of Texas-Arlington, for making the VSM available to us. The authors would also like to thank the anonymous reviewers for their suggestions to improve the quality of the manuscript.

References

1. B. Kim et al., "Tuning payload delivery in tumour cylindroids using gold nanoparticles," *Nat. Nanotechnol.* **5**(6), 465–472 (2010).
2. Y. Cheng et al., "Delivery and efficacy of a cancer drug as a function of the bond to the gold nanoparticle surface," *Langmuir* **26**(4), 2248–2255 (2010).
3. F. Petrelli, K. Borgonovo, and S. Barni, "Targeted delivery for breast cancer therapy: the history of nanoparticle-albumin-bound paclitaxel," *Expert Opin. Pharmacother.* **11**(8), 1413–1432 (2010).
4. X. Huang and M. A. El-Sayed, "Gold nanoparticles: optical properties and implementations in cancer diagnosis and photothermal therapy," *J. Adv. Res.* **1**(1), 13–28 (2010).
5. E. S. Day, J. G. Morton, and J. L. West, "Nanoparticles for thermal cancer therapy," *J. Biomech. Eng.* **131**(7), 074001–074005 (2009).
6. V. P. Zharov et al., "Photoacoustic flow cytometry: principle and application for real-time detection of circulating single nanoparticles, pathogens, and contrast dyes in vivo," *J. Biomed. Opt.* **12**(5), 051503 (2007).
7. E. I. Galanzha et al., "In vivo magnetic enrichment and multiplex photoacoustic detection of circulating tumour cells," *Nat. Nanotechnol.* **4**(12), 855–860 (2009).
8. N. W. Kam et al., "Carbon nanotubes as multifunctional biological transporters and near-infrared agents for selective cancer cell destruction," *Proc. Natl. Acad. Sci. U. S. A.*, **102**(33), 11600–11605 (2005).
9. C. J. Gannon et al., "Carbon nanotube-enhanced thermal destruction of cancer cells in a noninvasive radiofrequency field," *Cancer* **110**(12), 2654–2665 (2007).
10. X. Huang et al., "Plasmonic photothermal therapy (PPTT) using gold nanoparticles," *Lasers Med. Sci.* **23**(3), 217–228 (2008).
11. C. W. Lam et al., "A review of carbon nanotube toxicity and assessment of potential occupational and environmental health risks," *Crit. Rev. Toxicol.* **36**(3), 189–217 (2006).
12. Y. Zhao, G. Xing, and Z. Chai, "Nanotoxicology: are carbon nanotubes safe?," *Nat. Nanotechnol.* **3**(4), 191–192 (2008).
13. P. P. Simeonova, "Update on carbon nanotube toxicity," *Nanomedicine (Lond)* **4**(4), 373–375 (2009).
14. J. D. Byrne, T. Betancourt, and L. Brannon-Peppas, "Active targeting schemes for nanoparticle systems in cancer therapeutics," *Adv. Drug. Deliv. Rev.* **60**(15), 1615–1626 (2008).
15. A. K. Iyer et al., "Exploiting the enhanced permeability and retention effect for tumor targeting," *Drug Discovery Today* **11**(17–18), 812–818 (2006).
16. A. De la Zerda et al., "Carbon nanotubes as photoacoustic molecular imaging agents in living mice," *Nat. Nanotechnol.* **3**(9), 557–562 (2008).
17. A. Kumar et al., "Multifunctional magnetic nanoparticles for targeted delivery," *Nanomedicine* **6**(1), 64–69 (2010).
18. X. Fan et al., "Preparation and characterization of magnetic nanoparticles with radiofrequency-induced hyperthermia for cancer treatment," *Sheng Wu Yi Xue Gong Cheng Xue Za Zhi* **23**(4), 809–813 (2006).
19. A. Ito et al., "Medical application of functionalized magnetic nanoparticles," *J. Biosci. Bioeng.* **100**(1), 1–11 (2005).
20. A. Ito et al., "Heat-inducible TNF-alpha gene therapy combined with hyperthermia using magnetic nanoparticles as a novel tumor-targeted therapy," *Cancer Gene Ther.* **8**(9), 649–654 (2001).
21. D. B. Warheit et al., "Comparative pulmonary toxicity assessment of single-wall carbon nanotubes in rats," *Toxicol. Sci.* **77**(1), 117–125 (2004).
22. G. Jia et al., "Cytotoxicity of carbon nanomaterials: single-wall nanotube, multi-wall nanotube, and fullerene," *Environ. Sci. Technol.* **39**(5), 1378–1383 (2005).
23. X. Huang et al., "Determination of the minimum temperature required for selective photothermal destruction of cancer cells with the use of immunotargeted gold nanoparticles," *Photochem. Photobiol.* **82**(2), 412–417 (2006).
24. A. Welch, "The thermal response of laser irradiated tissue," *IEEE J. Quantum Electron.* **20**(12), 1471–1481 (1984).
25. S. L. Jacques and S. A. Prahl, "Modeling optical and thermal distributions in tissue during laser irradiation," *Lasers Surg. Med.* **6**(6), 494–503 (1987).
26. C. Sturesson and S. Andersson-Engels, "A mathematical model for predicting the temperature distribution in laser-induced hyperthermia. Experimental evaluation and applications," *Phys. Med. Biol.* **40**(12), 2037 (1995).
27. R. R. Letfullin et al., "Laser-induced explosion of gold nanoparticles: potential role for nanophotothermolysis of cancer," *Nanomedicine* **1**(4), 473–480 (2006).
28. V. P. Zharov et al., "Microbubbles-overlapping mode for laser killing of cancer cells with absorbing nanoparticle clusters," *J. Phys. D: Appl. Phys.* **38**(15), 2571 (2005).
29. V. Zharov et al., "Synergistic enhancement of selective nanophotothermolysis with gold nanoclusters: potential for cancer therapy," *Lasers Surg. Med.* **37**(4), 329–329 (2005).
30. A. A. Balandin, "Thermal properties of graphene and nanostructured carbon materials," *Nat. Mater.* **10**(8), 569–581 (2011).
31. L. Tong et al., "Gold nanorods mediate tumor cell death by compromising membrane integrity," *Adv. Mater.* **19**(20), 3136–3141 (2007).
32. B.-G. Wang et al., "In-vivo intratissue ablation by nanojoule near-infrared femtosecond laser pulses," *Cell Tissue Res.* **328**(3), 515–520 (2007).
33. J. Zhou et al., "A new strategy for prostate cancer with a small molecular therapy," *AACR Meeting Abstracts* **2006**(1), 515-d–516 (2006).
34. W. Lu et al., "Targeted photothermal ablation of murine melanomas with melanocyte-stimulating hormone analog-conjugated hollow gold nanospheres," *Clin. Cancer Res.* **15**(3), 876–886 (2009).
35. H. Huang, K. Rege, and J. J. Heys, "Spatiotemporal temperature distribution and cancer cell death in response to extracellular hyperthermia induced by gold nanorods," *ACS Nano* **4**(5), 2892–2900 (2010).
36. J. Riegler et al., "Magnetic cell delivery for peripheral arterial disease: a theoretical framework," *Med. Phys.* **38**, 3932 (2011).
37. A. Kanneganti et al., "Deep brain optogenetic stimulation using bessel beam," *Biophys. J.* **100**(3), Supp.1, 95a (2011).
38. Y. N. Mishra, N. Ingle, and S. K. Mohanty, "Trapping and two-photon fluorescence excitation of microscopic objects using ultrafast single-fiber optical tweezers," *J. Biomed. Opt.* **16**, (10), 105003 (2011).